Melvyn and Carolyn Miller Foundation for Innovation

Toward Spatial light modulation based on a fluidically actuated elastic sheet: dielectrophoretic-driven deformations of a lubricated elastic sheet

Israel Gabay[a], Amir Gat[a], Moran Bercovici[a]

[a]Faculty of Mechanical Engineering, Technion – Israel Institute of Technology, Israel

Abstract

We present an analytical, numerical, and experimental investigation of the deformations induced on a free liquid-air interface and a lubricated elastic sheet as a result of dielectrophoretic forces. We consider the case of interdigitated electrodes in two-dimensions and provide numerically validated closed-form solutions for the electric field and force distribution on the elastic sheet. Coupling these forces with the elasticity equation for the sheet and Reynolds' equation for the fluid, we provide solutions for the spatio-temporal evolution of deformation. We demonstrate experimentally the creation of such deformation on an oil-air interface and provide quantitative measurements using digital holography. We believe the concept and model provided may be useful for applications requiring dictated deformations such as adaptive optics and soft robotics.

1. Introduction

The ability to deform an elastic interface into a desired pattern has potential use in a wide range of applications, such as reconfigurable lab-on-a-chip devices[1], soft robotics[2], and adaptive optics[3]. A variety of mechanisms can be considered for achieving such elastic deformations, including piezoelectric, magnetic and pneumatic actuators. Fluidic-based actuation, i.e. where deformation is induced by a liquid in contact with the elastic sheet, is of particular interest as it allows deformations to be achieved without adding active elements to the elastic interface, and can thus also be used to deform liquid-liquid or liquid-gas interfaces. Furthermore, the two-way coupling of the dynamics of the fluid with those of the elastic interface can lead to an interesting flow patterns and novel instability phenomena.

The majority of studies on the deformation of a lubricated elastic sheet considered pressure-driven or gravity-driven flows[4–6]. Recently, work by Boyko et al[7] suggested the use of non-uniform electroosmotic flow as a mechanism for the creation of internal pressure gradients driving elastic deformations[8,9]. However, the pressures that could be obtained in such systems scale linearly with the electric field, leading to relatively low pressures.

Dielectrophoresis (DEP) is the behavior of dielectrics materials (insulators) due to the presence of a non-uniform electric field. DEP forces scale with the electric field squared, and have been demonstrated to be an effective method for manipulating discrete objects, particularly particles[10–12] and cells[13,14]. Brown et al[15] showed that DEP forces formed by a non-uniform electric field result in deformations of oil-air interface for thin films of oil. By using energy methods, they describe the dependence of the periodic amplitude of the deformations at steady state as a function of the fluids properties, fluid height and electrodes geometry[16]. However, to the best of our knowledge, no model exists for the dynamics of an elastic sheet due to DEP forces.

In this work, we present a theoretical model and experimental demonstration for the deformations of an elastic sheet suspended on a thin liquid layer due to an electric field established by electrodes at its surface. We provide an analytical expression for the electric field in a 3-layer configuration consisting of the liquid, elastic sheet, and air. Using the electric field, we analytically compute the force distribution on the sheet through Maxwell's stresses. Coupling this force with the viscous flow and elastic deformation in limits of small deformation and negligible inertial effects, we obtain an analytical solution for the deformation of the sheet in time. We use this expression to study the effects of permittivity, conductivity, electrode geometry, and electric frequency on the resulting deformation. We use digital holographic microscopy for real-time monitoring of deformations induced by an interdigitated electrode array covered by a film of oil, demonstrating the phenomenon and enabling characterization of the deformations in support of the theoretical model.

2. Anaytical and numerical investigation

2.1. Problem formulation and governing equations

As illustrated in Figure 1, we study the dynamics of an elastic sheet with length l_m, thickness h_m and electric permittivity ε_m suspended on top of a thin layer viscous fluid of density ρ, viscosity μ, electric permittivity ε_f, subjected to DEP forces. The liquid rests on a rigid surface patterned with interdigitated electrodes of length l_e and edge-to-edge gap l_g. We use a Cartesian coordinate system whose origin coincides with the surface of the plate. We assume that the thickness of the electrodes is negligible, so the electrode surface is considered to be at $\tilde{y}=0$. The electrical actuation of the electrodes generates a force on the sheet, and consequently, the elastic sheet is deformed. The elastic deformation is coupled to the viscous fluid flow in the chamber, giving rise to flows and pressure distributions. We define the gap between the rigid surface and the sheet (the fluid film thickness) as $\tilde{h}(\tilde{x},\tilde{t})=\tilde{d}(\tilde{x},\tilde{t})+h_0$, where $\tilde{d}(\tilde{x},\tilde{t})$ is the induced deformation and h_0 is the initial height. The fluid velocity and pressure are respectively $\tilde{\mathbf{u}}=\tilde{u}\hat{x}+\tilde{v}\hat{y}$ and $\tilde{p}$.

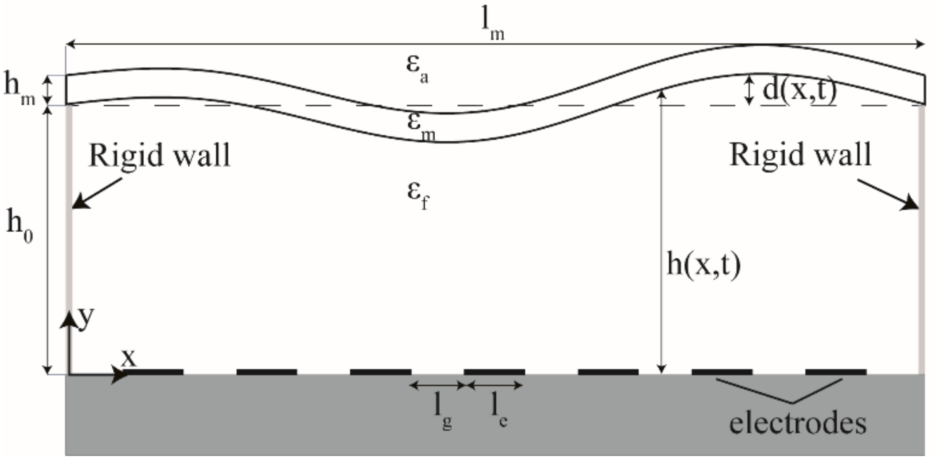

Figure 1. Schematic illustration of the investigated configuration. A thin liquid film is confined between a lower rigid plate containing interdigitated electrodes and an elastic sheet. The other side of the sheet is in contact with air. Actuation of the electrodes is expected to result in deformation of the elastic sheet.

We use l and h_0 to scale the horizontal and the vertical coordinates, (u',v') t', and p' to denote the characteristics velocities, time and pressure, respectively. The governing equations of the fluid flow under the assumption of a shallow geometry $(h_0/l=\varepsilon\ll 1)$, a small reduced Reynolds number $(\mathrm{Re}_r=\varepsilon^2\rho u'l/\mu\ll 1)$ and a small Womersley number $(Wo=\rho h_0^2/(\mu t')\ll 1)$ are the lubrication equations given by the continuity equation

(2.1) $$\tilde{\nabla}\cdot\tilde{\mathbf{u}}=0,$$

and the momentum equation in the $\tilde{x}$ and $\tilde{y}$ directions,

(2.2) $$\frac{\partial\tilde{p}}{\partial\tilde{x}}=\mu\frac{\partial^2\tilde{u}}{\partial\tilde{y}^2},\quad \frac{\partial\tilde{p}}{\partial\tilde{y}}=0.$$

The velocity boundary conditions on the bottom (rigid) surface are $\left.(u,v)\right|_{\tilde{y}=0}=(0,0)$ corresponding to no penetration and no-slip conditions. On the upper (elastic) surface, we also require no-slip and set a kinematic condition for the vertical velocity, $\left.(u,v)\right|_{\tilde{y}=\tilde{h}}=\left(0,\partial\tilde{h}/\partial\tilde{t}\right)$, according to the deformations of the sheet under the assumption of small deformations[17]. The solution of equation (2.2) yields a Poiseuille flow profile where the pressure is not known. Substituting it into equation (2.1) and integrating with respect to $\tilde{y}$ and using the velocity boundary conditions we obtain the well-known Reynolds equation,

(2.3) $$\frac{\partial\tilde{h}}{\partial\tilde{t}}=\frac{\partial}{\partial\tilde{x}}\left(\frac{\tilde{h}^3}{12\mu}\frac{\partial\tilde{p}}{\partial\tilde{x}}\right).$$

The governing equation of the deformation of the elastic sheet is derived by considering an infinitesimally small segment of the sheet, using the linear and angular momentum equations and assuming that the deformations of the membrane are much smaller than the characteristic length over which the deformation changes, $(\tilde{d}\ll l)$. The resulting equation is the transverse displacement of a beam[18],

(2.4)
$$-\tilde{B}\frac{\partial^4 \tilde{d}}{\partial \tilde{x}^4}+\tilde{T}\frac{\partial^2 \tilde{d}}{\partial \tilde{x}^2}-\rho_m g+\tilde{f}_e=\rho_m\frac{\partial^2 \tilde{d}}{\partial \tilde{t}^2}.$$

The first term on the LHS represents the bending term, where $\tilde{B}=E_Y I=E_Y h_m^3/12\left(1-\nu^2\right)$, E_Y is Young's modulus of the matter, I is the moment inertia of the cross-section of the elastic sheet and ν is the Poisson's ratio. The second term on the LHS represents the tension term, where $\tilde{T}=E_Y h_m(\partial\tilde{\upsilon}/\partial\tilde{x})$, $\tilde{\upsilon}$ is the longitudinal displacement. The third term is the gravity force where ρ_m is the mass density per unit length, and the last term $\tilde{f}_e$ represents the external forces exerted on the sheet in the y-direction that can be further decomposed into two terms: the fluid pressure, $\tilde{p}$, and the forces due to the electric field in the system i.e. $\tilde{f}_{DEP}$. The term on the RhS is the solid inertia.

In our analysis, we consider the cases in which the solids inertia and the gravitational force are negligible, and therefore equation (2.4) becomes,

(2.5)
$$\tilde{p}=\tilde{B}\frac{\partial^4 \tilde{d}}{\partial \tilde{x}^4}-\tilde{T}\frac{\partial^2 \tilde{d}}{\partial \tilde{x}^2}-\tilde{f}_{DEP}.$$

The derivatives of the deformation in space or time are equal to the fluid thickness derivative through the simple relation between them, $\tilde{h}(\tilde{x},\tilde{t})=\tilde{d}(\tilde{x},\tilde{t})+h_0$. Accordingly substituting equation (2.5) to equation (2.3) yields the viscous-elastic equation for the deformation,

(2.6)
$$\frac{\partial \tilde{d}}{\partial \tilde{t}}=\frac{\partial}{\partial \tilde{x}}\left(\frac{\tilde{h}^3}{12\mu}\frac{\partial}{\partial \tilde{x}}\left(\tilde{B}\frac{\partial^4 \tilde{d}}{\partial \tilde{x}^4}-\tilde{T}\frac{\partial^2 \tilde{d}}{\partial \tilde{x}^2}-\tilde{f}_{DEP}\right)\right).$$

To obtain a linear viscous-elastic equation we require the deformation to be much smaller than the initial fluid thickness, $\tilde{d}\left(\tilde{x},\tilde{t}\right)\ll h_0$ and obtain

(2.7)
$$\frac{\partial \tilde{d}}{\partial \tilde{t}}=\frac{h_0^3}{12\mu}\left(\tilde{B}\frac{\partial^6 \tilde{d}}{\partial \tilde{x}^6}-\tilde{T}\frac{\partial^{24} \tilde{d}}{\partial \tilde{x}^4}-\frac{\partial^2 \tilde{f}_{DEP}}{\partial \tilde{x}^2}\right).$$

We normalize equation (2.7) with the following parameters, $\tilde{x}=x\frac{l}{2}$ where $l=l_e+l_g$, $\tilde{y}=yh_0$, $\tilde{d}=dh_0$, $\tilde{h}=hh_0$, $\tilde{t}=tt'$, $\tilde{f}_{DEP}=f_{DEP}f'$, and we obtain,

(2.8)
$$\frac{\partial d}{\partial t}+\frac{h_0^3 t'}{12\mu l^2}\left(-\frac{32\tilde{B}}{l^4}\frac{\partial^6 d}{\partial x^6}+\frac{16\tilde{T}}{l^2}\frac{\partial^4 d}{\partial x^4}\right)=-\frac{\varepsilon^2 t' f'}{3\mu}\frac{\partial^2 f_{DEP}}{\partial x^2},$$

the characteristics time and DEP force will be determined later. Both terms inside the parentheses are restoring terms, and the working regime of the system can be determined by performing scaling analysis on those terms. We define $\delta=2\tilde{B}/\tilde{T}l^2$ as a nondimensional parameter representing the ratio between the bending and the tension in the system. For $\delta\gg 1$, the bending dominates over tension and we can neglect the tension term, whereas for $\delta\ll 1$ we are in tension regime. The characteristic time scale can be obtained by balancing the dominant term with the temporal term, yielding

(2.9) $$t'_T = \frac{3\mu l}{4\tilde{T}\varepsilon^3},\ \ t'_B = \frac{3\mu l^3}{8\tilde{B}\varepsilon^3},$$

where t'_T, t'_B are the tension and bending time scales respectively, and for the general case where $\delta \approx O(1)$ we can work with either of the time scales. Equation (2.8) has a sixth order spatial derivative and a first-order time derivative, hence, we need six boundary conditions and one initial condition. The initial condition is zero deformation at $t = 0$. As shown in Figure 1, the system is a closed chamber with rigid walls at the two boundaries. Therefore, we require that at the boundary there will be no deformation, $\tilde{d} = 0$, no moments, $\partial^2\tilde{d}/\partial\tilde{x}^2 = 0$, and zero volume flux which through an integration of the velocity profile with respect to $\tilde{y}$ dictates $\partial\tilde{p}/\partial\tilde{x} = 0$. We express the last condition in terms of the deformation by applying $\partial/\partial\tilde{x}$ on equation (2.5) and substituting the pressure derivative. In summary, the BCs are,

(2.10) $$\tilde{d} = 0,\qquad \frac{\partial^2\tilde{d}}{\partial\tilde{x}^2} = 0,\qquad \frac{\partial}{\partial\tilde{x}}\left(\tilde{B}\frac{\partial^4\tilde{d}}{\partial\tilde{x}^4} - \tilde{T}\frac{\partial^2\tilde{d}}{\partial\tilde{x}^2} - \tilde{f}_{DEP}\right) = 0,\quad \text{at } \tilde{x} = 0, l_m \text{ and } \tilde{t} \geq 0.$$

Finally, we need to express the actuating force inducing the deformations. The governing equation of the force density on a dielectric subjected to an electric field was first derived by Helmholtz and is known as the Korteweg-Helmholtz body force[19],

(2.11) $$\tilde{\mathbf{f}} = \rho_f\tilde{\mathbf{E}} - \frac{1}{2}\tilde{E}^2\tilde{\nabla}\varepsilon_i + \frac{1}{2}\tilde{\nabla}\left(\rho\frac{\partial\varepsilon}{\partial\rho}\tilde{E}^2\right),$$

where $\mathbf{E}$, ρ_f, ε_i, ρ are the electric field, the free charge density, the electric permittivity and the mass density respectively. The first term of the force is simply the Coulomb force on free charges which, since we assume our system to be electroneutral everywhere, is negligible. By assuming incompressibility of the liquid, the last term, the electrostriction is be negligible as well. Therefore, the only dominant term is the second one, which also vanishes everywhere except for at the interfaces between the liquid, elastic sheet, and air. In order to obtain this force, we must first solve for the distribution of the electric field.

2.2. Electric field solution

2.2.1. Analytical solution

To obtain the force field applied on the membrane, we first solve the electric field distribution inside the system. Figure 2a presents a schematic description of the problem, consisting of three distinct regions having different permittivities – the liquid, the membrane, and the air. We solve the Laplace equation for the electric potential in these three regions. Separation of variables yields a solution of the type

(2.12) $$\tilde{\phi}_i = \sum_{n=0}^{\infty}\cos\left(\tilde{k}_n\tilde{x}\right)\left[\tilde{A}_{i,n}\exp\left(\tilde{k}_n\tilde{y}\right) + \tilde{B}_{i,n}\exp\left(-\tilde{k}_n\tilde{y}\right)\right],\ \ i = \{fluid, membrane, air\}$$

where $\tilde{A}_{i,n}, \tilde{B}_{i,n}, \tilde{k}_n$ are determined from the boundary and continuity conditions. The conditions that relate the different areas are the continuity of the electric potential and the displacement field,

$$\tilde{\phi}_i = \tilde{\phi}_j, \quad \varepsilon_i \partial \tilde{\phi}_i / \partial \tilde{y} = \varepsilon_j \partial \tilde{\phi}_j / \partial \tilde{y}, \tag{2.13}$$

at the liquid-sheet and air-sheet interface, $\tilde{y} = h_0;\ \tilde{y} = h_0 + h_m$, wherein the indices i and j indicate the liquid and the membrane for the lower interface and the membrane and the air for the upper interface. On the left boundary, we prescribe symmetry condition, $\partial \tilde{\phi} / \partial \tilde{x} = 0$ and on the right boundary we prescribe anti-symmetry condition, $\tilde{\phi} = 0$. Far from the electrodes, for $y \to \infty$, we require that the electric potential vanishes, $\tilde{\phi} = 0$, and at the electrodes surface, $\tilde{y} = 0$, we assume a fixed potential distribution[20],

$$\tilde{\phi}_0(x) = \begin{cases} V_0 & 0 < \tilde{x} < l_e / 2 \\ V_0 \left(l_e + l_g - 2\tilde{x}\right) / 2 & l_e / 2 < \tilde{x} < \left(l_e + l_g\right) / 2 \end{cases}. \tag{2.14}$$

It is convenient to scale the system using the following parameters

$$\begin{aligned} &\tilde{\phi} = \phi V_0,\ \tilde{A}_{in}, \tilde{B}_{in} = \left(A_{in}, B_{in}\right) \cdot V_0,\ R_{mf} = \frac{\varepsilon_m}{\varepsilon_f},\ R_{am} = \frac{\varepsilon_a}{\varepsilon_m} \\ &\tilde{x} = x\frac{l}{2},\ \tilde{y} = y\frac{l}{2},\ \tilde{k}_n = k_n \frac{2}{l},\ l_e = \alpha_e l,\ l_g = \left(1 - \alpha_e\right) l,\ h_0 = \alpha_0 l,\ h_m = \alpha_m l \end{aligned},$$

where $\alpha_e, \alpha_0, \alpha_m$ are constants defining the ratios between the different length scales of the problem. R_{am}, R_{mf} are the ratios between the air and membrane permittivity and the membrane and liquid permittivity. We note that for the purpose of the electric field solution, we normalize the $\tilde{y}$ coordinate with the length scale of the $\tilde{x}$ coordinate, l. This will simplify the electric potential and field solutions. The non-dimensional solution then takes the form

$$\phi_i = \sum_{n=0}^{\infty} \cos\left(k_n x\right)\left[A_{in} \exp\left(k_n y\right) + B_{in} \exp\left(-k_n y\right)\right], \tag{2.15}$$

And the electric field distribution is obtained from the potential using the relation $\left(E_x, E_y\right) = -\nabla \phi$,

$$\begin{aligned} E_x &= \sum_{n=0}^{\infty} k_n \cos\left(k_n x\right)\left[A_{in} \exp\left(k_n y\right) + B_{in} \exp\left(-k_n y\right)\right] \\ E_y &= \sum_{n=0}^{\infty} k_n \cos\left(k_n x\right)\left[A_{in} \exp\left(k_n y\right) - B_{in} \exp\left(-k_n y\right)\right] \end{aligned}. \tag{2.16}$$

Figure 2b and 2c present the resulting non-dimensional equipotential lines and electric field lines, respectively. For clarity of presentation, the images present four solution domains which have been 'stitched' together in accordance with the boundary conditions.

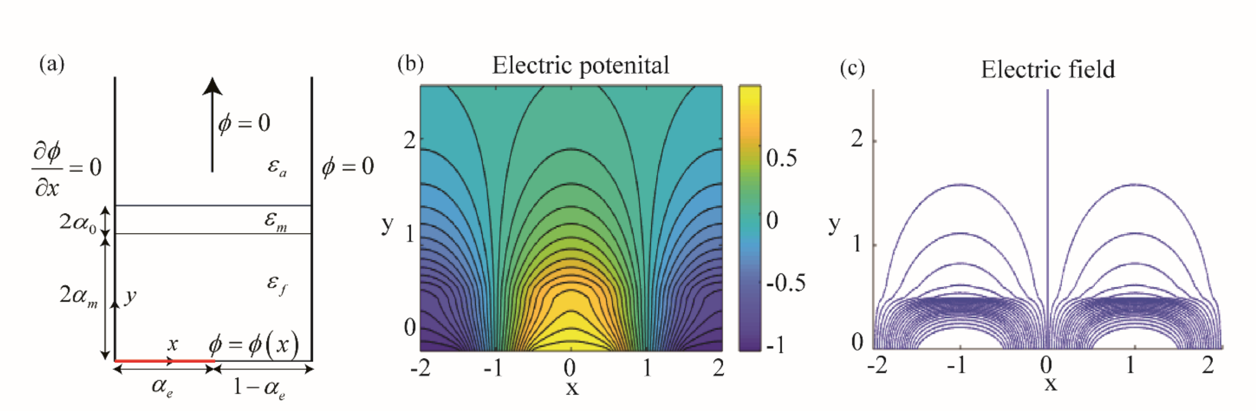

Figure 2 – Analytical solution of the electric potential in a three-layer structure (liquid, membrane, air), generated by an array of periodic electrodes immersed in the liquid. (a) Schematic of the problem formulation showing one cell of the infinite array of electrodes along with key parameters and boundary conditions for the solution. The lower area (fluid) the middle (membrane) and the upper (air) have electric permittivities of ε_f, ε_m *and* ε_a, *respectively. The non-dimensional fluid and membrane thickness are* $2\alpha_0$, *and* $2\alpha_m$, *and the non-dimensional electrode length and gap are* α_e, *and* $1-\alpha_e$ *respectively. The boundary condition on the left side is periodicity and on the right side is symmetry. At y=0 there is a prescribed potential distribution given by the electrodes, and far from the electrodes, the field vanishes. (b,c) Electric potential and electric field distributions of the analytical solution, shown over four cells joined together for better illustration of the solution. The* x *and* y *axes are normalized by the length of one cell,* $(l_e + l_g)/2$. *The ratio of permittivities between the membrane and the fluid is* $R_{mf} = 0.2$ *and for the membrane and the air is* $R_{am} = 0.4$. *The lengths of the electrode and of the gap between the electrodes are equal,* $\alpha_e = 0.5$ *and the normalized fluid and membrane thickness are respectively* $\alpha_0 = 1/4$, *and* $\alpha_m = 1/20$.

2.2.2. Numerical solution

To validate our analytical solution, we also solve the Laplace equation using an in-house finite difference numerical simulation based on the Jacobi scheme for elliptic equations,

$$\phi_{i,j}^{k+1} = \frac{1}{2(1+\beta^2)}\left[\phi_{i-1,j}^{k} + \phi_{i+1,j}^{k} + \beta^2\left(\phi_{i,j-1}^{k} + \phi_{i,j+1}^{k}\right)\right]. \tag{2.17}$$

where the i, j subscripts denote the spatial indices in the x and y-axes, respectively, and the k superscript represents the iteration number. $\beta = \Delta x / \Delta y$ and $\Delta x, \Delta y$ are the spatial steps in x and y-direction respectively. For simplicity, we chose $\beta = 1$ and solve for the case of $\alpha_m = 0$.

We interface the three domains through the boundary conditions (2.13), with continuity of the displacement field taking the form

$$\phi_{i,j_{in}}^{k} = \frac{R_{af}\phi_{i,j_{in}+1}^{k} + \phi_{i,j_{in}-1}^{k}}{R_{af}+1}. \tag{2.18}$$

Table 1 - Summary of the numerical scheme for different y locations. The general scheme valid almost everywhere except one row below the interface, one row above the interface and the interface itself. The scheme solves for the entire domain (not including the boundaries).

y location	Numerical scheme
$j = j_{in} - 1$	$\phi^{k+1}_{i,j_{in}-1} = \frac{1}{4}\left[\phi^{k}_{i-1,j_{in}-1} + \phi^{k}_{i+1,j_{in}-1} + \phi^{k}_{i,j_{in}-2} + \frac{R_{af}\phi^{k}_{i,j_{in}+1} + \phi^{k}_{i,j_{in}-1}}{R_{af}+1}\right]$
$j = j_{in}$	$\phi^{k+1}_{i,j_{in}} = \frac{1}{4}\left[\frac{R_{al}\phi^{k}_{i+1,j_{in}+1} + \phi^{k}_{i+1,j_{in}-1}}{R_{al}+1} + \frac{R_{al}\phi^{k}_{i-1,j_{in}+1} + \phi^{k}_{i-1,j_{in}-1}}{R_{al}+1} + \phi^{k}_{i,j_{in}-1} + \phi^{k}_{i,j_{in}+1}\right]$
$j = j_{in} + 1$	$\phi^{k+1}_{i,j_{in}+1} = \frac{1}{4}\left[\phi^{k}_{i-1,j_{in}+1} + \phi^{k}_{i+1,j_{in}+1} + \frac{R_{af}\phi^{k}_{i,j_{in}+1} + \phi^{k}_{i,j_{in}-1}}{R_{af}+1} + \phi^{k}_{i,j_{in}+2}\right]$
$j \neq j_{in} - 1, j_{in}, j_{in} + 1$	$\phi^{k+1}_{i,j} = \frac{1}{4}\left[\phi^{k}_{i-1,j} + \phi^{k}_{i+1,j} + \phi^{k}_{i,j-1} + \phi^{k}_{i,j+1}\right]$

We use first-order forward finite difference for the derivative of the potential in the air and backward finite difference for the fluid. j_{in} represents the index value of the interface in the y direction and is defined as $j_{in} \triangleq 2\alpha_0 / \Delta y + 1$. R_{af} represents the permittivity ratio between the air and the fluid. We summarize the complete scheme without the boundary conditions in Table 1.

As illustrated in figure 3a, for further simplification of the numerical solution,we define our domain as consisting of two adjacent cells, thus replacing the Neumann condition which would have been required at the symmetry plane (marked as '3') with a Dirichlet condition on the other external face (marked as '2'). Table 2 lists the boundary conditions on each of the boundaries. The initial potential distribution is set to zero everywhere except on the first boundary as shown in Table 2. The scheme is then solved iteratively to convergence.

Table 2 - Dirichlet boundary conditions after the extension of the numerical domain. Boundary 1 is the electrode surface, boundaries 2 and 4 are the right and left edges respectively and boundary 3 is the air potential far from the electrode.

Boundary No	indexes	Electric potential
1	$j = 1, \forall i$	$\phi = \begin{cases} (1+x)/(1-a); & -1 < x < -a \\ 1; & -a < x < a \\ (1-x)/(1-a); & a < x < 1 \end{cases}$
2	$\forall j, i = N_x$	$\phi = 0$
3	$j = N_y, \forall i$	$\phi = 0$
4	$\forall j, i = 1$	$\phi = 0$

We define the convergence criterion as, $e > \left\| \phi^{k+1} - \phi^{k} \right\|_{\infty} / \left\| \phi^{k+1} \right\|_{\infty}$, where the infinite norm is defined as $\left\| A \right\|_{\infty} = \max\left(\sum_{j=1}^{n} \left| A_{1,j} \right|, \sum_{j=1}^{n} \left| A_{2,j} \right|, \ldots, \sum_{j=1}^{n} \left| A_{m,j} \right| \right)$.

The result of the numerical simulation is in good agreement with the analytical solution, as shown in Figure 3. Figure 3b and 3c present a side-by-side comparison of the analytical and numerical solution of the potential field for a 121x301 grid with electric permittivity ratio between the air and the fluid, $R_{af} = 0.2$. Equal electrodes length, electrodes gap, and fluid thickness, $\alpha_e = \alpha_0 = 0.5$ and convergence criterion, $e = 10^{-8}$, showing excellent qualitative agreement. Figure 3d presents the potential distribution at the fluid-air interface at $y = 2\alpha_0$ showing also excellent quantitative agreement. The analytical expression for the electric field, (2.12), is thus validated and we can use it to calculate the DEP force an elastic membrane.

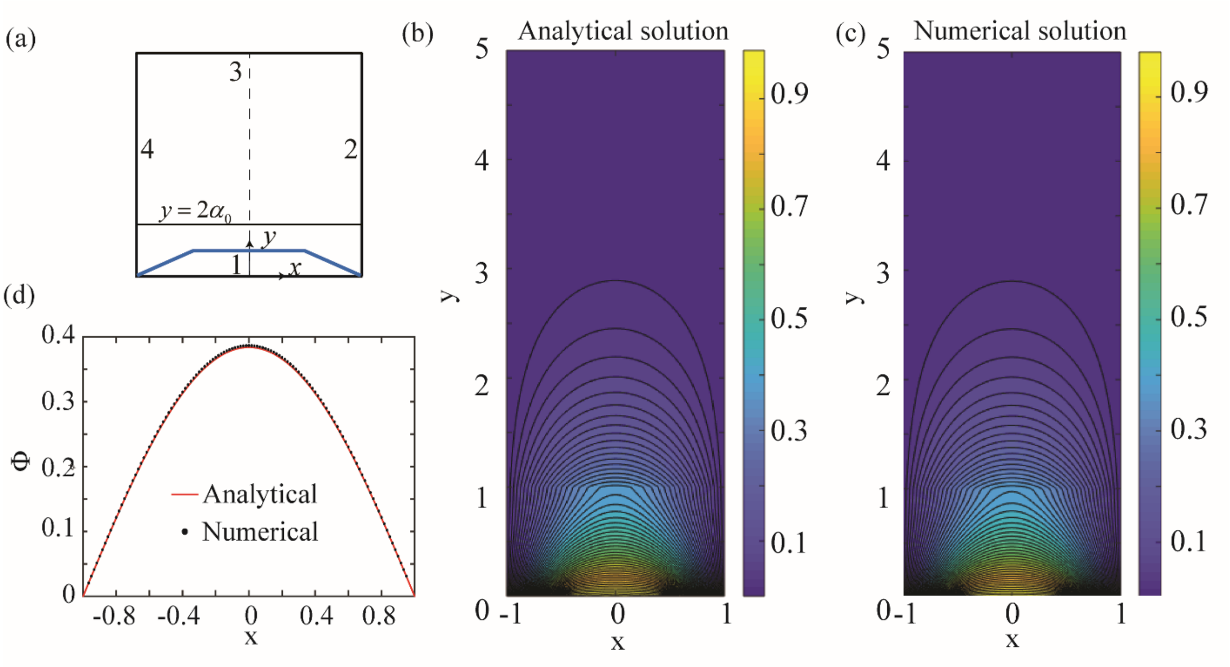

Figure 3 – Numerical simulation of the electric potential distribution in two neighboring cells. The membrane thickness is equal to zero, $\alpha_m = 0$. The fluid thickness, the electrodes length and the electrodes gap are equal, $\alpha_e = \alpha_0 = 0.5$, and the electric permittivity ratio between the air and the fluid is $R_{af} = R_{am} R_{mf} = 0.2$. (a) Schematic of the computational domain used for the simulation. The boundary numbering corresponds to the boundary conditions as listed in Table 2, the blue line represents the potential distribution on the bottom (at $y = 0$) where at the electrode surface $\phi = 1$. (b,c) analytical and numerical solution of the electrical potential shown over two cells joined together for easier visualization. (d) Comparison of the analytical and numerical potential distributions at the liquid-air interface $\left(y = 2\alpha_0 \right)$. The relative error between the analytical and numerical model is less than 1%.

2.3. DEP forces on the elastic sheet

After solving for the electric field distribution, we need to derive an expression for the force on the membrane, the RHS of equation (2.8). As we mentioned in section 2.1 the body force vanishes almost everywhere except at the interfaces of the membrane. Figure 4a presents the control volumes that contain the upper and lower interfaces of the membrane. For convenience, the integral around each of the edges can be replaced through the divergence theorem by an equivalent surface integral on the edges of the control volume over an equivalent tensor, the Maxwell stress tensor,

(2.19) $$T_{ij}=\varepsilon E_i E_j-\frac{\varepsilon}{2}\delta_{ij}E_k E_k \ .$$

After integration we obtain

(2.20) $$\tilde{f}_{DEP}\left(\tilde{x}\right)=\frac{1}{2}\left[\left(\varepsilon_f\,\tilde{E}_x^2\Big|_{\tilde{y}=h_0^+}+\varepsilon_m\,\tilde{E}_y^2\Big|_{\tilde{y}=h_0^+}\right)\left(1-R_{mf}\right)+\left(\varepsilon_m\,\tilde{E}_x^2\Big|_{\tilde{y}=\left(h_0+h_m\right)^+}+\varepsilon_a\,\tilde{E}_y^2\Big|_{\tilde{y}=\left(h_0+h_m\right)^+}\right)\left(1-R_{am}\right)\right],$$

where $\tilde{E}_x\Big|_{\tilde{y}=h_0^+}$ represents, for example, the x-direction component of the electric field at the upper interface of the membrane that is exposed to the air. Figure 4b presents the normalized DEP force distribution on the membrane $f_{DEP}=\tilde{f}_{DEP}/\left(4V_0^2\varepsilon_a/l^2\right)$.

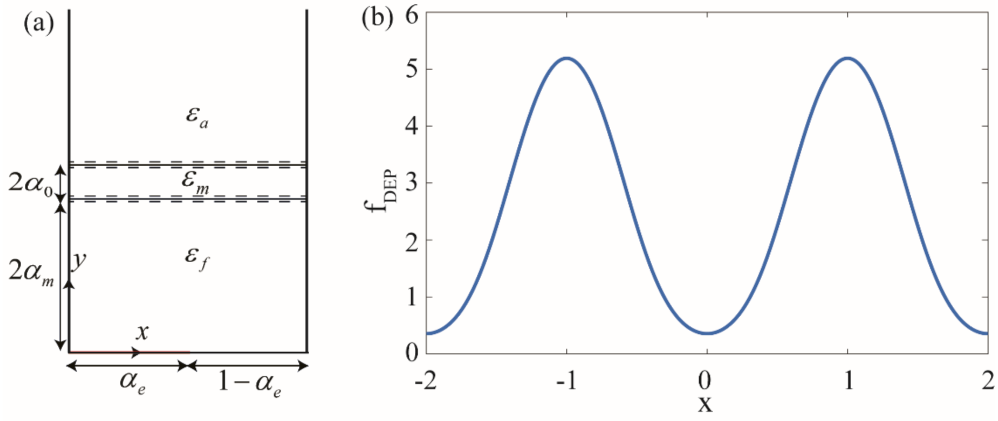

Figure 4 – DEP force distribution on the membrane. (a) Schematic illustration of one cell of the system. We define two infinitesimally thin control volumes at the interfaces of the membrane. By integrating the stress tensor on the surface of the two control volumes, we derive the DEP force on the membrane. Outside of the control volume on the membrane, the force is equal to zero due to the uniformity of the permittivity in each region. (b) Normalized force distribution on the membrane at the y-direction. The force is a function of the different permittivities, the thickness of the fluid film, the thickness of the membrane and the applied voltage. However, the direction of the force is determined only by the permittivities, in this case $\varepsilon_f>\varepsilon_m>\varepsilon_a$*, and as expected from (2.20) the force is positive everywhere.*

2.4 Free surface deformations

Once we have an expression for the DEP force at the interface, consider the limit case of a free surface configuration $\left(\alpha_m=0\right)$ of n cells, each $l/2$ in length. The solution we obtained for the electric field and therefore also for the DEP force valid for an infinite number of electrodes, accordingly the forces at the edges aren't accurate. Hence, to simplify the solution, we consider two empty cells for each side of the chamber and considered the force there to be zero. We can simplify our governing equation, (2.8), by defining the membrane tension to be the fluid surface tension $\tilde{T}=\gamma$, dropping the bending term $\tilde{B}=0$, and substituting in the previously derived expression for the tension time scale $t_T' = \frac{3\mu l}{4\tilde{T}\varepsilon^3}$. Our equation now takes the form of

(2.21)
$$\frac{\partial d}{\partial t}+\frac{\partial^4 d}{\partial x^4}=-\frac{V_0^2\varepsilon_a}{l\gamma\varepsilon}\frac{\partial^2 f_{DEP}}{\partial x^2}.$$

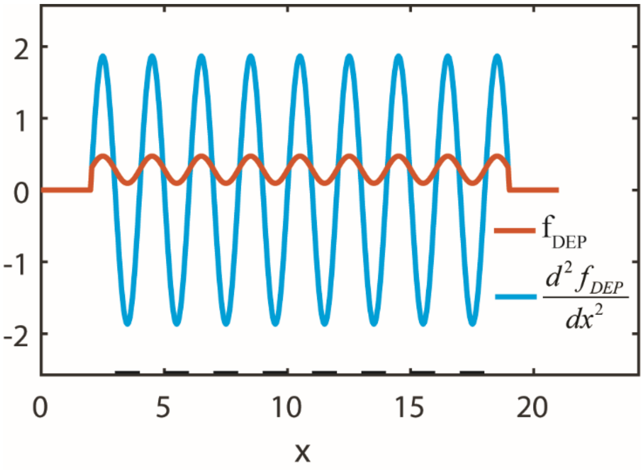

Figure 5 – Analytical results showing the DEP force distribution on an air-fluid interface having a permittivity ratio of $R_{af}=2/5$*. The non-dimensional height of the fluid is* $\alpha_0=1/2$*, and the length of the chamber is 21 cells. The electrode denoted by the black lines on the x-axis. The blue line is the DEP force distribution inside the chamber and the red line is the second derivative of the DEP force, which serves as the source term for the elastic equation (2.21) when the non-dimensional is set to one.*

We assume that the fluid start at rest, i.e. $d(x,t=0)=0$ and that the fluid pressure is zero at the edges[21], i.e. the side walls of the chamber are open and connected to big reservoirs such that, fluid can flow in and out. At the boundaries, we require no deformation, and using equation (2.5) and substituting the pressure and the force we obtain zero spatial derivative of the deformation at the edges. In summary, the boundary conditions are,

(2.22)
$$d=0,\quad \frac{\partial^2 d}{\partial x^2}=0,\quad \text{at } x=0,n \text{ and } t\geq 0.$$

The general solution using the Green function[22] for this equation using such homogenous boundary conditions is given by

(2.23)
$$d(x,t)=\int_0^n f_i(\xi)G(x,\xi,t)d\xi+\int_0^t\int_0^n \Phi(\xi,\tau)G(x,\xi,t-\tau)d\xi d\tau.$$

f_i is the initial deformation that in our case is zero so the left integral vanishes. Φ is the source term of the equation which in our case is $\Phi = -\left(\partial^2 f / \partial x^2\right)\cdot\left[\left(V_0^2\varepsilon_a\right)/\left(l\gamma\varepsilon\right)\right]$, and the Green function itself is given by

(2.24) $$G\left(x,\xi,t\right)=\frac{2}{n}\sum_{m=1}^{\infty}\sin\left(\lambda_m\xi\right)\sin\left(\lambda_m\xi\right)\exp\left(-\lambda_m^4 t\right),$$

where $\lambda_m = \dfrac{\pi m}{n}$ are the eigenvalues of the problem. By substituting the DEP force and the Green function, (2.24), to equation (2.23) we obtain the general solution for the deformations of the fluid-air interface,

(2.25) $$d\left(x,t\right)=\sum_{m=1}^{\infty}\frac{-16n^5\left(1-\mathrm{e}^{-\frac{m^4\pi^4}{n^4}t}\right)\left(R_{af}-1\right)^2\left(\sin\left[\frac{2m\pi}{n}\right]+\sin\left[\frac{19m\pi}{n}\right]\right)\sin\left[\frac{m\pi x}{n}\right]}{m^4\left(m^2-n^2\right)\pi^5 R_{af}\left(\cosh\left[\alpha_0\pi\right]+R_{af}\sinh\left[\alpha_0\pi\right]\right)^2}.$$

Figure 6 presents the deformation $d\left(x,t\right)$ for $R_{af}=2/5$, $\alpha_0 = 1/4$, $n=21$, and $V_0^2\varepsilon_a / l\gamma\varepsilon = 1$, using the first 50 terms of the series. For the singular term at $m=n$, we derived the limit of $m \to n$ and added it to the sum. The form of the exponential term (scaling to the fourth power of the wave number) in (2.25) provides insight on the dynamic behavior of the deformation. The short waves account for the deformations at short times while the long waves account for the deformations at much longer times.

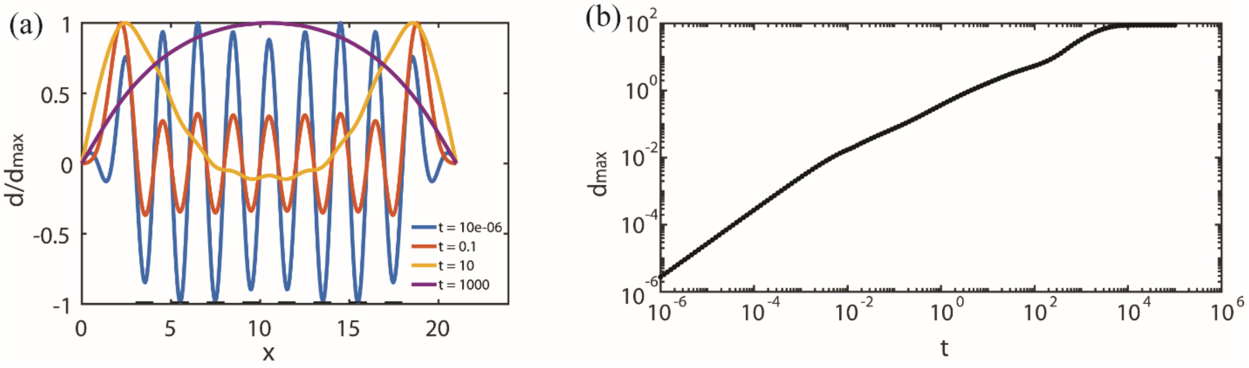

Figure 6 – Analytical results showing the deformation of the fluid-air interface due to DEP actuation. (a) The spatial deformations of the interface at different time points. At short times high wave numbers dominate the deformation, while long times are dominated by low wave numbers. (b) The maximum magnitude of deformation along with the chamber as a function of time. The system reaches a steady state at $t \approx 10^4$

3.Experimental investigation

3.1 Chip fabrication

Figure 7a shows a typical device containing three independent microfluidic chambers defined by structured SU8 layer. Each chamber comprises an interdigitated electrode array electrically insulated by a dielectric layer, with different width of the electrodes and different gaps between them. The electrodes are connected to an external power supply through the electrical pads located at one edge of the device. Figure 7b shows the microfabrication process flow. All the microfabrication steps are performed in a clean room of class 1000. We used double-polished 4” borofloat glass (WRS materials) wafers as a substrate. We define the metal structures by a lift-off process, depositing a sandwiched metal layer of 15 nm Ti - 30 nm Pt - 15 nm Ti by physical evaporation (BAK501, Evatec AG). We use two layers of titanium to improve the adhesion of the metal layers to both the substrate and the dielectric; the platinum layer is used because it is resistant to hydrofluoric acid (HF) and acts as a stopping layer during the etching process for opening the electrical connections (see below). The final metal thickness is 60 nm. We then deposit 500 nm of silicon oxynitride (SiON) followed by a deposition of 100 nm of silicon dioxide (SiO2) as a dielectric layer by plasma-enhanced chemical vapor deposition (PECVD). We then expose the electrical pads by etching the dielectric over them by using HF. Finally, we deposit a 40 µm-thick layer of SU8 (SU8 1060, Gersteltec) by spinning it for 40 s at 700rpm and define the lateral walls of the microfluidic structure by a standard lithographic step (3). We dice the wafer to singulate the devices with dimensions of approximately 2 × 1 cm.

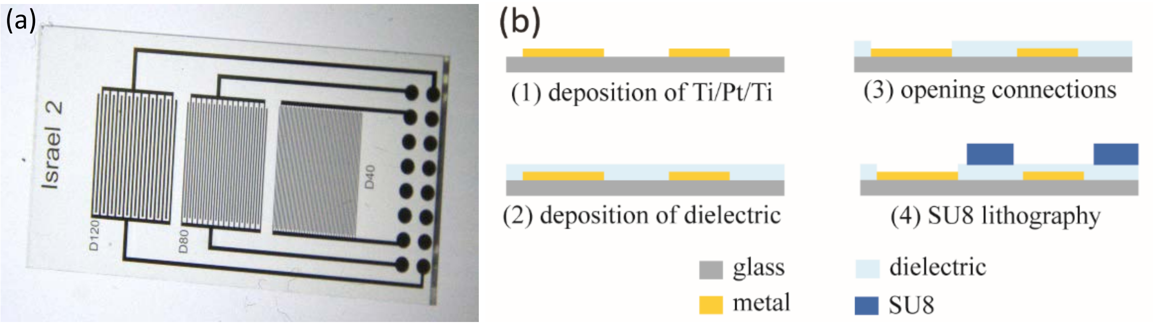

Figure 7. Device fabrication. (a) Image of a typical device used in this work. The device is composed of a substrate patterned with integrated electrodes and several independent microfluidic chambers. The interdigitated electrodes cover the total area of each chamber and are connected through conducting lines to pads at the perimeter of the device, providing an interface to the power supplies. We insulate the electrodes by a dielectric layer while leaving the electrical pads exposed. We use a layer of SU8 to define the lateral walls of each microfluidic chamber. (b) Schematic of the microfabrication process flow. 1. We define the metal structures (15 nm Ti / 30 nm Pt / 15 nm Ti) on a glass substrate by a standard lift-off process. 2. We deposit a dielectric layer via PECVD. 3. We open the electrical connections (the pad electrodes) by wet or dry etching. 4. Using a lithography step we define the microfluidic chambers with a 40 µm thick layer SU8 photoresist.

3.2. Experimental setup

We measure free-surface deformations of low viscosity silicone oil (317667, SIGMA-ALDRICH) in response to DEP forces, for different actuation voltages. We use interdigitated electrodes where the width of each one of them is $20\mu m$ and the gap between them is $180\mu m$. The electrodes array covered by a thin dielectric layer form a 7.5 mm X 7.5 mm open chamber geometry on top of which we place $1\mu l$ of the dielectric fluid. The electric potential on the electrodes is generated by a high-voltage power supply (2410, Keithley). To spread the fluid over the chamber we apply a 400 V potential difference between the electrodes until the fluid wets the entire chamber and then turn off the voltage. The final thickness of the oil is approximately 18 um. To deform the liquid-air interface we apply again a potential difference between the electrodes and observe the deformations. We measure the deformations using reflection digital holographic microscope (DHM-R1000, Lyncee tec) from above, creating a hologram image by interference between the reference beam and the reflected beam from the object. We extract the topographic information of the surface from the phase image of the interference pattern.

3.3 Experimental results

Ideally, the deformation would be measured by measuring the reflection from the liquid-air interface. However, stronger reflections are obtained from the bottom glass surface. We, therefore, focus on the glass surface, and the information collected by the DHM corresponds to the change in phase as light travels through the liquid which has a higher index of refraction than the air. Figure 8 presents the results of the experiments for different applied voltages, where the black lines on Figure 8b indicate the location of the electrodes. The minimum deformation is obtained precisely above the electrode's center, as predicted by the theory. The deformation shows non-linear behavior with the applied voltage, though weaker than the E^2 behavior expected from theory. For example, changing the voltage from 200V to 250V results in an amplitude increase in a factor of 1.7. This might be due to the non-linearity of equation (2.6) where the deformation is not so small compare to the initial fluid thickness or the distribution of the electric field that changed as a result of the fluid-air interface deformations and therefore the DEP force changed too which are not accounted for in the model.

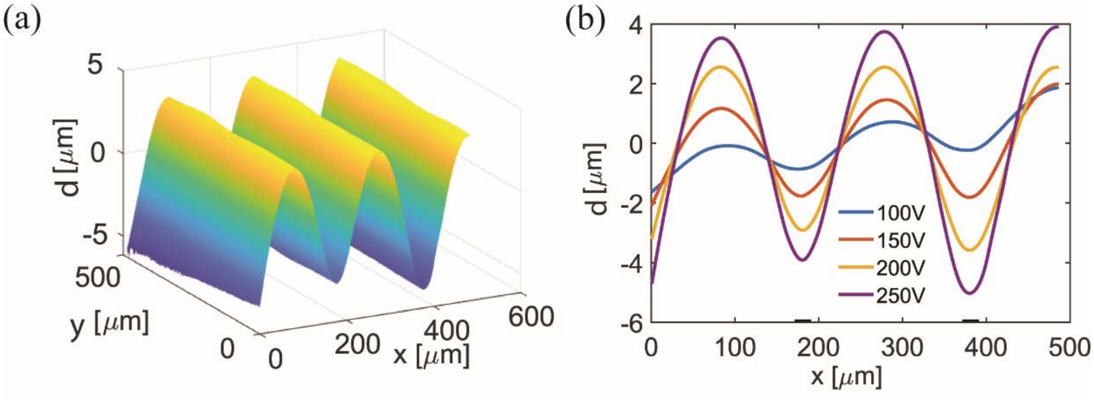

Figure 8. *Experimental measurements of the fluid-air interface in response to the electric field established by interdigitated electrodes (a) Topographic image of the interface at 250 V. The wavelength of the deformation is equal to the pitch of the electrodes,* $200\mu m$. *The maximum deformation is obtained above the gaps between the electrodes. (b) The deformation along the center of the membrane perpendicular to the electrodes, for different voltages.*

References

1. Thorsen, T., Maerkl, S. J. & Quake, S. R. Microfluidic Large-Scale Integration. *Science* **298**, 580–584 (2002).
2. Trivedi, D., D. Rahn, C., M. Kier, W. & D. Walker, I. Soft Robotics: Biological Inspiration, State of the Art, and Future Research. *Applied Bionics and Biomechanics* (2008).
3. Mishra, K., Van den Ende, D. & Mugele, F. Recent Developments in Optofluidic Lens Technology. *Micromachines* **7**, 102 (2016).
4. Hosoi, A. E. & Mahadevan, L. Peeling, Healing, and Bursting in a Lubricated Elastic Sheet. *Phys. Rev. Lett.* **93**, 137802 (2004).
5. Hewitt, I. J., Balmforth, N. J. & Bruyn, J. R. D. Elastic-plated gravity currents. *European Journal of Applied Mathematics* **26**, 1–31 (2015).
6. Chronis, N., Liu, G. L., Jeong, K.-H. & Lee, L. P. Tunable liquid-filled microlens array integrated with microfluidic network. *Opt. Express, OE* **11**, 2370–2378 (2003).
7. Boyko, E., Rubin, S., Gat, A. D. & Bercovici, M. Flow patterning in Hele-Shaw configurations using non-uniform electro-osmotic slip. *Physics of Fluids* **27**, 102001 (2015).
8. Rubin, S., Tulchinsky, A., Gat, A. D. & Bercovici, M. Elastic deformations driven by non-uniform lubrication flows. *Journal of Fluid Mechanics* **812**, 841–865 (2017).
9. Boyko, E., Eshel, R., Gommed, K., Gat, A. D. & Bercovici, M. Elastohydrodynamics of a pre-stretched finite elastic sheet lubricated by a thin viscous film with application to microfluidic soft actuators. *Journal of Fluid Mechanics* **862**, 732–752 (2019).
10. Squires, T. M. Particles in electric fields. *Fluids, Colloids and Soft Materials: An Introduction to Soft Matter Physics* 59–79 (2016).
11. Jones, T. B. *Electromechanics of particles*. (Cambridge University Press, 1995).

12. Morgan, H. & Green, N. G. *AC electrokinetics: colloids and nanoparticles*. (Research Studies Press, 2003).

13. Gascoyne, P. R., Wang, X.-B., Huang, Y. & Becker, F. F. Dielectrophoretic separation of cancer cells from blood. *IEEE transactions on industry applications* **33**, 670–678 (1997).

14. Pohl, H. A. & Crane, J. S. Dielectrophoresis of Cells. *Biophysical Journal* **11**, 711–727 (1971).

15. Brown, C. V., Wells, G. G., Newton, M. I. & McHale, G. Voltage-programmable liquid optical interface. *Nature Photonics* **3**, 403–405 (2009).

16. Brown, C. V., Al-Shabib, W., Wells, G. G., McHale, G. & Newton, M. I. Amplitude scaling of a static wrinkle at an oil-air interface created by dielectrophoresis forces. *Applied Physics Letters* **97**, 242904 (2010).

17. Leal, L. G. *Advanced Transport Phenomena: Fluid Mechanics and Convective Transport Processes*. (Cambridge University Press, 2007).

18. Howell, P., Ockendon, J. & Kozyreff, G. *Applied solid mechanics*. (Cambridge University Press, 2009).

19. Stratton, J. A. *Electromagnetic Theory*. (McGraw-Hill, 1941).

20. Morgan, H., Izquierdo, A. G., Bakewell, D., Green, N. G. & Ramos, A. The dielectrophoretic and travelling wave forces generated by interdigitated electrode arrays: analytical solution using Fourier series. *Journal of Physics D: Applied Physics* **34**, 1553 (2001).

21. Kodio, O., Griffiths, I. M. & Vella, D. Lubricated wrinkles: Imposed constraints affect the dynamics of wrinkle coarsening. *Phys. Rev. Fluids* **2**, 014202 (2017).

22. Poli͡anin, A. D. *Handbook of linear partial differential equations for engineers and scientists*. (Chapman & Hall/CRC, 2002).